Nano Energy 38 (2017) 313–325

Contents lists available at ScienceDirect

Nano Energy

journal homepage: www.elsevier.com/locate/nanoen

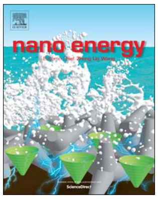

Full paper

Switchable heat transfer mechanisms of nucleation and convection by wettability match of evaporator and condenser for heat pipes: Nano-structured surface effect

Xianbing Ji[a], Jinliang Xu[a,*], Hongchuan Li[a], Guohe Huang[b]

[a] *The Beijing Key Laboratory of Multiphase Flow and Heat Transfer, North China Electric Power University, Beijing 102206, PR China*
[b] *MOE Key Laboratory of Regional Energy and Environmental Systems Optimization, North China Electric Power University, Beijing 102206, PR China*

ARTICLE INFO

Keywords:
Heat pipe
Wettability
Nano-surface
Phase distribution
Heat transfer mechanism

ABSTRACT

A novel strategy was proposed for the improvement of vapor chamber heat pipe (HP) performance. The mastoid process array, wettability control of heat pipe and control of liquid charged into heat pipe are comprehensively used to manage the phase distribution. Thus, the two dominant heat transfer mechanisms of nucleation and convection can be switched. The objective of this strategy is to maintain nucleation mechanism but suppress convection mechanism. Holding the nucleation mechanism, our newly developed heat pipe behaves excellent thermal sensitivity with respect to heating loads. Our idea was thoroughly verified by experiments, in which three HP samples were fabricated and tested: #1 equal wettability sample, #2 moderate wettability difference sample and #3 opposite wettability sample. The wettability difference was generated with nano-structured surface. The #1 sample shows convection mechanism with heat transfer coefficients (HTCs) not changed versus heat fluxes, due to evaporator porous wick occupied by larger vapor content and liquid filmwise condensation on condenser surface. The super-hydrophilic evaporator and super-hydrophobic condenser (#3 sample) shows nucleation mechanism with HTCs significantly increased with increases in heat fluxes, due to large driving force to flood evaporator porous wick by water and expose condenser by vapor. Surprisingly, opposite wettability match HP had overall thermal resistances of only 1/3 to those of equal wettability HP. The comprehensive use of mastoid process array and controls of wettability and water amount charged into HP lowers heater temperatures by 30–40 °C at high heat fluxes such as ~100 W/cm^2 on a large heater area of 1.4 cm^2, paving a new road for heat pipe performance improvement.

1. Introduction

Heat pipe dissipates heat from a high heat flux chip for electronic cooling. Inefficient phase change heat transfer increases the heater surface temperature and shortens the device lifetime [1]. At ultra-high heat flux, dry-out may occur to burnout the device [2]. Heat pipe involves both boiling and condensing, which have been extensively investigated. In 1950–1980s, due to the demand to develop high power density nuclear power plant, phase change heat transfer was studied on metal surface and in large size channels, under pool, passive or forced convective conditions [3]. The theory framework was established, including bubble or droplet nucleation, dynamics, flow pattern, heat transfer coefficient (HTC), flow instability and critical heat flux (CHF). Abundant data were collected to support the theory development [4]. Before 2000, enhanced heat transfer techniques including features in millimeter or sub-millimeter scale, such as fins, grooves and textures, or wicking materials, were developed [5]. Since then, with the increased availability of micro/nano fabrication technologies, and new materials, there has been an increased focus on boiling and condensing in micron/nano scale, including modified surface wettability [6–8]. Phase change heat transfer with micro/nano structures is a hot research topic [9,10].

Heat pipe combines boiling and condensing heat transfer together. It has been widely used in industries due to its simple geometry and passive characteristic. For modern electronic cooling, heat pipe shall dissipate ~100 W heating load on a square centimeter area [11], or heat flux attaining ~500 W/cm^2 for hotspot (for instance, one square millimeter area) [12]. The chip temperature should be lower than 85 °C and CHF shall not occur [13]. A flat plate heat pipe is expected to satisfy the challenging requirements.

Different from separated effects of boiling and condensing, heat pipe couples the two processes. Boiling or condensing results for

---

[*] Corresponding author.
E-mail address: xjl@ncepu.edu.cn (J. Xu).

http://dx.doi.org/10.1016/j.nanoen.2017.06.010
Received 28 February 2017; Received in revised form 31 May 2017; Accepted 5 June 2017

separated effects are difficult to be directly used for heat pipes. These results are performed in a controlled way. Pool boiling happens under the condition that the heater is immersed by liquid. Condensation is also widely investigated in a controlled manner at given pressure and vapor velocity. However, for a heat pipe, the phase distribution and parameters such as vapor pressure and temperature are not only dependent on evaporator, but also dependent on condenser. The term of phase distribution refers to the vapor and liquid distribution in a void space not occupied by solid material. For two-phase flow and heat transfer, a specific point in a void space is either occupied by vapor or by liquid. The information of phase distribution tells us where is liquid and where is vapor. First, the evaporator and condenser coupling influences the vapor pressure and temperature in heat pipes. At given vapor temperature, the heater temperature can be determined for specific heating load. A poor condenser performance weakens the vapor condensation to raise the vapor temperature. This in turn, increases the vapor temperature to lift the heater surface temperature, which is not expected for heat pipe. Second, the evaporator and condenser coupling influences the phase distribution in the void space (not occupied by solid material). If one uses hydrophobic evaporator and hydrophilic condenser, the liquid circulation becomes difficult and the heater is easy to be dried out, while the (liquid) film condensation deteriorates condenser performance. Thus, phase distribution is a key factor to influence the phase change heat transfer in heat pipes, but it has not been received much attention in the past.

The effect of wettabilities on heat pipe performance is reported in refs. [14–17]. The original contribution of this paper is summarized as follows. *Switchable heat transfer mechanisms*: The fresh idea was proposed for the improvement of heat pipe performance. Here, we comprehensively use the mastoid process array, wettability control of heat pipe and control of liquid charged into heat pipe, to manage the phase distribution, so that the two dominant heat transfer mechanisms can be switched. The objective of this strategy is to maintain nucleation mechanism but suppress convection mechanism. Holding the nucleation mechanism, our newly developed heat pipe behaves excellent thermal sensitivity with respect to heating loads. Heat transfer coefficients for both evaporator and condenser are significantly increased at high heating loads. The idea was thoroughly verified by our experiments. The use of hydrophilicity/hydrophobicity combination only is not sufficient to switch the two heat transfer mechanisms. The switchable heat transfer mechanisms of heat pipes are not reported previously. *Heat pipe configuration:* We used the biporous wick evaporator coupled with condenser surface. The mastoid process contains several lengths scale to coordinate various conflicts between capillary pressure and viscous resistance. Ji et al. [14] and Zhang et al. [15] dealt with oscillation heat pipe with snake-shaped capillary tube as the structure. Boreyko and Chen [16] investigated flat plate heat pipe having two parallel plates integrated together. Our heat pipe configuration is different from these references. *Liquid circulation in heat pipes:* Liquid circulation in heat pipe is a key factor to influence its performance. In our study, liquid return from condenser to evaporator involves not only the droplets coalescence induced jumping/capture process, but also the liquid suction process from tips of mastoid processes towards evaporator wick. Oscillation heat pipe works due to the pulsating flow induced fluid transport [14,15]. Liquid is transferred to evaporator by the droplet jumping in Boreyko and Chen [16].

We start from using the mastoid process array on a porous sub-layer as the basic evaporator structure. The porous sub-layer is directly sintered on copper surface. The mastoid process is a biporous structure, enhancing boiling heat transfer with separated length scales. Small pores (~1 μm scale, depending on particle size) between metallic particles generate capillary pressure for liquid suction. The sintering process generates large pore channels, having their width of 10–100 μm and even longer length. Size and number density of pore channels depend on pore former content. Pore channels can be generated even without pore former involved. They are helpful to reduce the viscous resistance for fluid transport. The available pool boiling experiments using mastoid process array showed significant enhancement of HTC and CHF [18]. However, if the mastoid process array is used in heat pipes, the capillary pressure should be significantly increased because liquid supply towards evaporator is more difficult than pool boiling condition. Xiao et al. [19] noted that for water, the capillary pressure is around ~10 kPa for micron sized pores, but it can be increased to ~100 kPa for nanopores such as ~100 nm, inspiring us to perform the nano-surface modification.

In this paper, comparative experiments were conducted using three heat pipe samples (Table 1) (#1 equal wettability sample, #2 moderate wettability difference sample, and #3 opposite wettability sample). Our results did show that two heat transfer mechanisms (nulceation and convection) can be switched by different matches of wettability of evaporator and condenser, due to the different phase distributions. The #1 sample shows the convection mechanism. On the contrary, the #3 sample shows the nucleation mechanism to behave the best performance. At q_e=100.3 W/cm^2 on a 1.4 cm^2 heater surface, the heater temperature is only 65.9 °C for #3 sample, which is 37.3 °C lower than that for #1 sample at the same heat flux. Surprisingly, the overall thermal resistance for #3 sample is only 1/3 of that for #1 sample, highlighting the great benefit by using super-hydrophilic evaporator and super-hydrophobic condenser to manage the water distribution and suppress the convection effect in heat pipes. The proposed strategy opens a new way to improve the heat pipe performance.

Table 1
The three heat pipe samples.

	Evaporator	Condenser	Remark	Abbreviation
#1	Particle sintering without nano	Plain surface without nano	Hydrophilic evaporator + hydrophilic condenser	IE-IC
#2	Particle sintering with nanosheet	Plain surface without nano	Super-hydrophilic evaporator + hydrophilic condenser	SIE-IC
#3	Particle sintering with nanosheet	Copper surface with nanograss	Super-hydrophilic evaporator + super-hydrophobic condenser	SIE-SOC

2. Materials and method

2.1. The strategy for wettability match and water charging amount

Phase distribution and heat transfer can be controlled not only by wettability, but also by charged liquid amount in HP (see Fig. 1). Here, three HP samples are identical in all aspects including the charged water mass, except different wettability matches. The #1 sample had a basic structure without nano-surface modification. Because the same material (copper) is used for both evaporator and condenser, the #1 sample contains hydrophilic evaporator and hydrophilic condenser (called equal wettability sample: IE-IC). The static contact angle is about 77° on a cleaned/polished copper surface, noting that the porous wick using particle sintering without nano-surface has larger capability to suck water than smooth plate surface. The #2 sample contains super-hydrophilic evaporator and hydrophilic condenser (called moderate wettability difference sample: SIE-IC). Inside the evaporator porous wick is with nano-surface modification, but the condenser is without nano-fabrication. The #3 sample had super-hydrophilic evaporator and super-hydrophobic condenser (called opposite wettability sample: SIE-SOC).

The mastoid process array forms the evaporator. Each tip of the mastoid process directly contacts the plain condenser surface. The mastoid process functions as (1) heat transfer enhancement, (2) liquid suction from condenser to evaporator, (3) supporting structure for heat

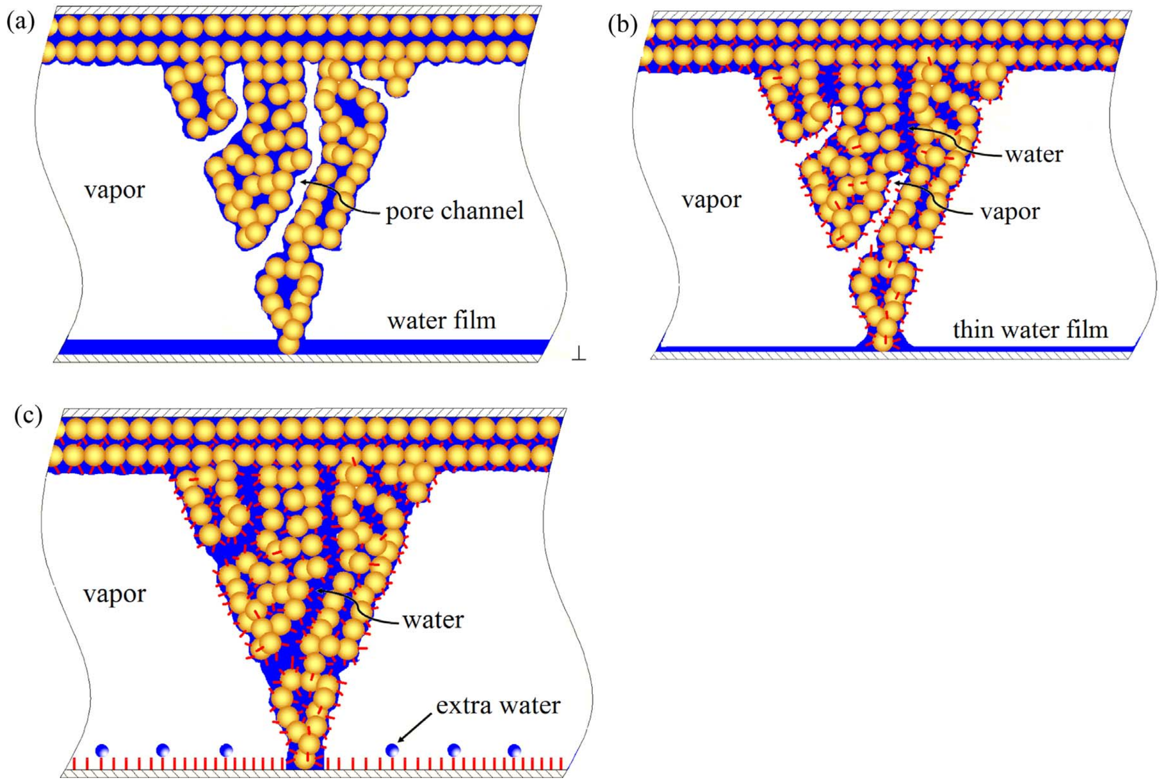

Fig. 1. Effect of wettability match of evaporator and condenser on phase distribution in heat pipe (a: #1 equal wettability sample, pore channels are occupied by vapor and condenser surface is covered by water film; b: #2, moderate wettability sample; c: #3, the porous wick is thoroughly flooded by water, the condenser surface is exposed by vapor except some droplets there. Note that the same amount of water is charged in three heat pipes.).

pipe. The mastoid process had several length scales of pore cavities. For mastoid process without nano-structure, two major length scales exist: small pores in ~1 μm between particles, acting as capillary pressure generation and nucleation sites. Larger pore cavities (or say pore channels) between parallel particle clusters are in ~10–100 μm scale to reduce viscous resistance for phase transportation. For mastoid process with nano-structure, additional nano-scale is introduced to significantly lift capillary pressure for liquid collection from condenser to evaporator wick. The hydrophobic condenser wall had the roughness of ~10–100 nm scale. The classical bubble nucleation criterion for boiling [20,21] and droplet nucleation criterion for condensing [22,23] showed that the micro/nano structures for our present heat pipe samples satisfy such criteria (see Section 3.3 for details).

Fig. 1c shows an ideal combination of super-hydrophilic evaporator and super-hydrophobic condenser for #3 sample. At the adiabatic condition, all the water stays in the evaporator porous wick and other locations are occupied by vapor. The nucleation mechanism is maintained to ensure increased HTCs at higher heat fluxes. If the same amount of water is charged into #1 HP sample (see Fig. 1a), some pore channels of mastoid process array are occupied by vapor, forming vapor-liquid interface on which convection evaporation happens. The convection mechanism also dominates on the condenser surface due to water film there. The convection mechanism makes HTCs not sensitive to applied heat fluxes. Fig. 1b shows the moderate wettability difference of evaporator and condenser, in between those shown in Fig. 1a and c. We shall note that, heating causes some vapor voids in the evaporator mastoid processes to expel identical volume of water out of the mastoid processes. This yields extra water re-distributed outside of the mastoid processes, which will be explained later.

Now, we discuss how to determine the optimal charge ratio, at which all the evaporator porous wicks are occupied by liquid but other locations except mastoid processes are occupied by vapor. Such situation is similar to the pool boiling for the heater sufficiently immersed in water. Theoretically, the condenser surface should be covered by pure vapor without liquid. Based on this analysis, we determined the optimal charge ratio in two steps (deionized water was the working fluid). Initially, in the atmospheric environment, we used the needle ejection to drip fine water drops on the dry evaporator wick gradually, noting the evaporator not covered by condenser cover. The dripping quantity was carefully recorded, and dripping process was stopped when tiny water drop began to fall down for the vertically positioned evaporator. Thus, the porous wick is sufficiently wet and all the non-condensable gas was expelled out of the porous wick.

The next step verifies the initially determined charge ratio. The charge process was performed for a dry HP under a vacuum pressure of ~0.06 Pa by a molecular pump. After each charge, the HP performance was checked by recording the heater temperature at different heat fluxes. The optimal charge ratio was reached at which the heater yielded the lowest temperature among several charge ratios, approaching the initially determined value. This is because the integrated HP needs additional water to be attached on the HP side walls.

Fig. 2 shows the effect of water charge ratios (φ) on evaporator wall temperatures at the center point ($T_{e,c}$). The results are given at two heat fluxes of 71.4 W/cm^2 and 28.3 W/cm^2. The curves display quasi-parabola shape. Both #1 and #3 samples had the lowest evaporator wall temperatures at the water charge ratio of about 30%, which is larger than the dripping test determined value by about 15%. Deviating from the optimal charge ratio increased evaporator wall temperatures. The finally determined water volume of 3.6 ml was charged into the whole heat pipe sample. The following discussions are based on heat pipes operating at the optimal charge ratio.

2.2. The three heat pipe samples

Mastoid process array widely appears in nature plant. Fig. 3a-c shows super-hydrophilic anubias barteri, Calathea zebrina and ruellia microstructure surfaces. They have large capability to absorb water. For instance, a 0.5 μl water droplet finishes the spreading process in a

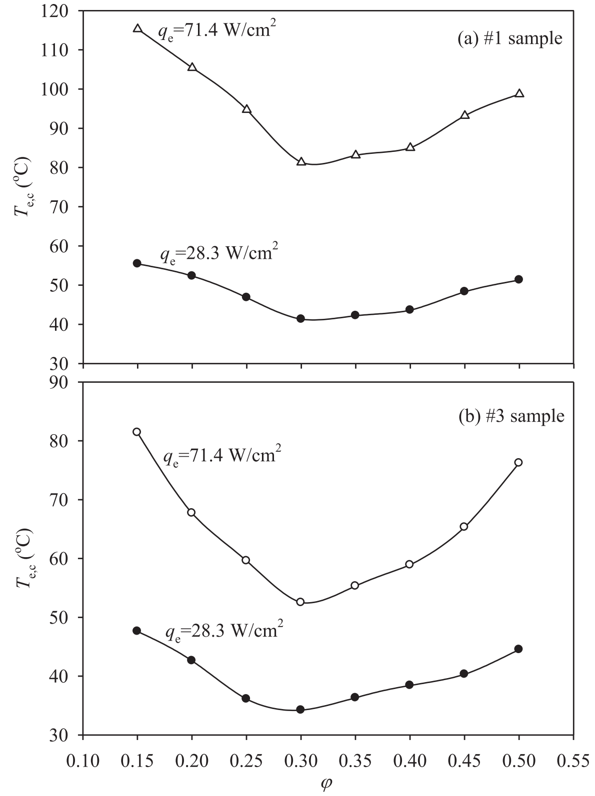

Fig. 2. Effects of water charge ratios on evaporator wall temperatures at the center point.

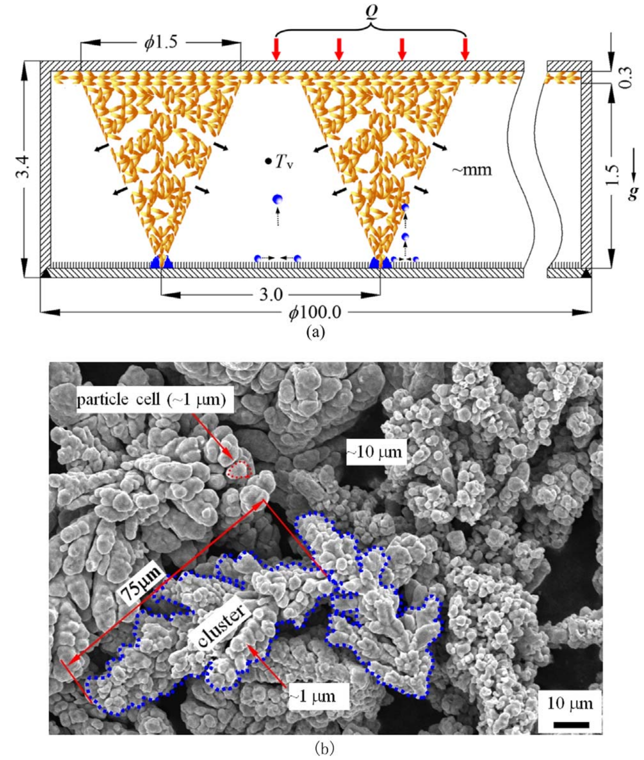

Fig. 4. Integrated flat plate heat pipe dimensions (a) and raw tree-branch shape copper particles before sintering for HP.

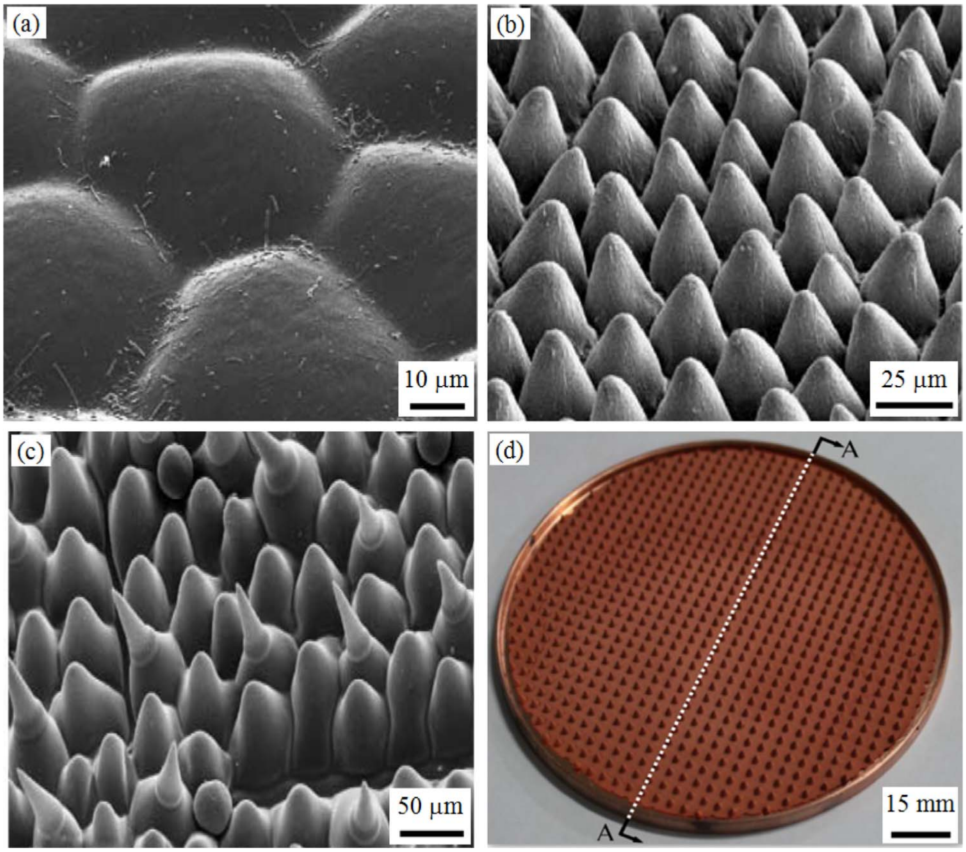

Fig. 3. Mastoid process array in nature (a: anubias barteri, b: Calathea zebrina, c: Ruellia devosiana) and newly fabricated evaportor with mastoid process array structure (d).

short time of 0.2 s on ruellia surface [24]. These surfaces can also be self-cleaned. When they contact a mixture of water and contamination particles, water is preferred to be attracted by the surface to form a water film, separating the surface from the dust particles [25]. The particles will be flushed away with the development of the spreading water film. Fig. 3d shows the evaporator containing the mastoid process array, whose shape is similar to those shown in Fig. 3a–c. However, microstructures not only exist on the surface, but also inside the mastoid process, that is different from those shown in Fig. 3a–c.

Fig. 4a shows the dimensions of the three HP samples. HP had an overall diameter of 100.0 mm and a thickness of 3.4 mm. The evaporator wall receives a heating load Q and the heat is dissipated to environment on the condenser wall. The evaporator contains a sub-porous layer with a thickness of 0.3 mm and mastoid process array. Each mastoid process had a base diameter of 1.5 mm and a height of 1.5 mm. The center distance between two neighboring mastoid processes is 3.0 mm. There are 710 mastoid processes over a 100 mm diameter surface.

There are two types of particles for industry applications: spheric powder and tree-branch powder. They are fabricated by different methods. We used the tree-branch particles, also called the electrolytic copper powder (see Fig. 4b before sintering). There are two sizes characterizing the particles: particle cell size and tree-branch size, which are about ~1 μm and 75 μm, respectively. Different particle cells are connected mechanically with each other to form the tree-branch. The connection is caused by the copper atom crystallization and coalescence of particle cells during the electrolyzation process. Tree-branch powders have two benefits for HPs: the gap between particle cells is in micron or sub-micron scale to generate larger capillary pressure; mechanical connection reduces thermal conductivity resistance. For randomly stacked tree-branch particles, larger gaps are formed between neighboring tree-branches (or call clusters).

The sintering process was performed with the help of a graphite mould in an oven under vacuum pressure. The sintering temperature and procedure were carefully controlled. Fig. 5a-d shows the sintering outcomes of the tree-branch powders without nano-structure for #1 HP evaporator. Two levels of sizes exist: ~1 μm small pore, and ~10–100 μm pore cavities. The structure is similar to cavern in shape. The #2-3 HP evaporators are with nano-structured surface (see Fig. 5e–f). After the sintering process, the nano-surface was made by immersing the sample in a 30% volume concentration H_2O_2 solution (hydrogen peroxide) by 8 h. After the samples are taken out of the oven, they are rinsed by deionized water and then baked in an oven at 60 °C temperature.

The nano-surface modification of the evaporator porous wick involved two steps. We suspended the evaporator with the internal mastoid processes array immersed in a liquid solution. The outer wall surface was in the air to keep such surface dry. The liquid was HNO_3 solution at a weight concentration of 15%. The immersion process lasted 15 min to remove oxidation film from the particle surface. Then, the sample was rinsed by de-ionized water and baked in an oven for 10 min at 60 °C. The second step was to immerse the mastoid processes array in a H_2O_2 solution with a 30% weight concentration by eight hours. The fabrication process was over after the rinsing by water and drying in the oven. Changing the weight concentrations of liquid solution and immersion time altered the nano-structure parameters such as nano-wire height, diameter and gap size between neighboring nano-wires.

Now we discuss the condenser surface. Fig. 6a-b shows the hydrophilic surface with CA=77° (#1–2 HP condenser), and the super-hydrophobic surface with CA=160° (#3 HP condenser), respectively. The nano-structure fabrication included two steps. The first step immersed the cleaned/polished copper surface in a 0.03 mol/l concentration ammonia solution by 96 h, took the sample out of the solution and then rinsed the sample by deionoized water, turning the hydrophilic surface to super-hydrophilic. The second step immersed the sample in a 0.5% mass content 1H,1H,2H,2H-perfluorodecyl-triethoxysilane ($C_{16}H_{19}F_{17}O_3Si$) solution by 1 h. Then, the sample was baked in an oven at 110 °C. The second step switched the sample from super-hydrophilic to super-hydrophobic, displaying the nano-flower shape on the surface (see Fig. 6b). The nano-surface modification process can be seen in refs. [26,27]. Experimental setup and data reduction can be seen in the supplementary material. Heat load Q had the uncertainty of 0.1 W. Temperature measurement had the uncertainty of 0.2 °C. The standard error propagation theory yielded the uncertainty of 5.5% for evaporator thermal resistance and 6.2% for condenser thermal resistance. Heat transfer coefficients had the uncertainties of 5.6% for evaporator and 6.3% for condenser.

2.3. Characterization of wettability of evaporator and condenser

Fig. 7 shows a smooth flat and a roughed surface. The Wenzel model [28] notes $\cos\alpha_w = r\cos\alpha$, where α_w is the contact angle (CA) between liquid and roughed surface, α is the CA between liquid and smooth surface and r is the "roughness factor" defined as

$$r = \frac{\text{actual surface}}{\text{geometric surface}} \tag{1}$$

The nano-sheet structure is assumed to have a cross section of $a \times b$ and a height of H. The distance between neighboring nano-sheets is c. The roughness factor r is

$$r = 1 + \frac{2(a+b)H}{(a+c)(b+c)} \tag{2}$$

With example values of H=210 nm, a=20 nm, b=100 nm and c=70 nm, r is 4.39. A hydrophilic smooth flat surface with α=77° becomes a super-hydrophilic surface with α_w=7.9°. Fig. 7c shows a smooth sphere surface just like a 10 μm particle, while Fig. 7d shows the roughed sphere surface just like nano-surface modification on the particle surface. Because the particle size is several magnitudes larger than the nano-structure characteristic size, the wettability on the curved surface is identical to the flat surface. That is, Fig. 7a and Fig. 7c have identical wettability, and Fig. 7b and Fig. 7d have identical wettability, respectively.

The term of "contact angle" is only suitable when liquids can be accumulated on specific location of a surface. This term is not suitable for the complete wetting condition, under which the contact angle approaches zero. The spreading time characterizes the surface wettability for super-hydrophilic surface. Instead, for the mastoid process evaporator encountered in this paper, water can be thoroughly sucked into the porous wick even without nano-surface modification, the suction time is used to characterize the wettability of hydrophilic porous medium, which is defined as the time from the initial contact between liquid and porous wick to the end of the suction process. The shorter the suction time, the more hydrophilic the porous medium is. Therefore, water droplet suction was tested in atmospheric environment under gravity (θ=0°) and against gravity (θ=180°). The samples are initially dry. A droplet with a diameter of 1.9 mm (3.6 μl volume) was gently deposited on the mastoid process tip. We define V_o as the volume outside of the conical mastoid process boundary (see Fig. 8a for the super-hydrophilic porous suction process, and Fig. 8b for V_o versus time t). At θ=0°, the super-hydrophilic porous (SIE sample) only needs 10 ms to absorb the water. The suction time is about one half of that for the hydrophilic IE sample, indicating the super-adsorption capability of the porous wick with nano-surface. The gravity effect on the water adsorption is small. For SIE sample, the against gravity at θ=180° prolongs the suction time by about 30% compared with θ=0°. The capillary pressure is the driving force. Gravity force is the driving force at θ=0° but becomes resistance at θ=180°. The suction test indicates the capillary pressure as the dominant driving force over the gravity force. For the condenser surface, the contact angle is 77° on the smooth surface and it is 160° on the surface with nano-surface modification.

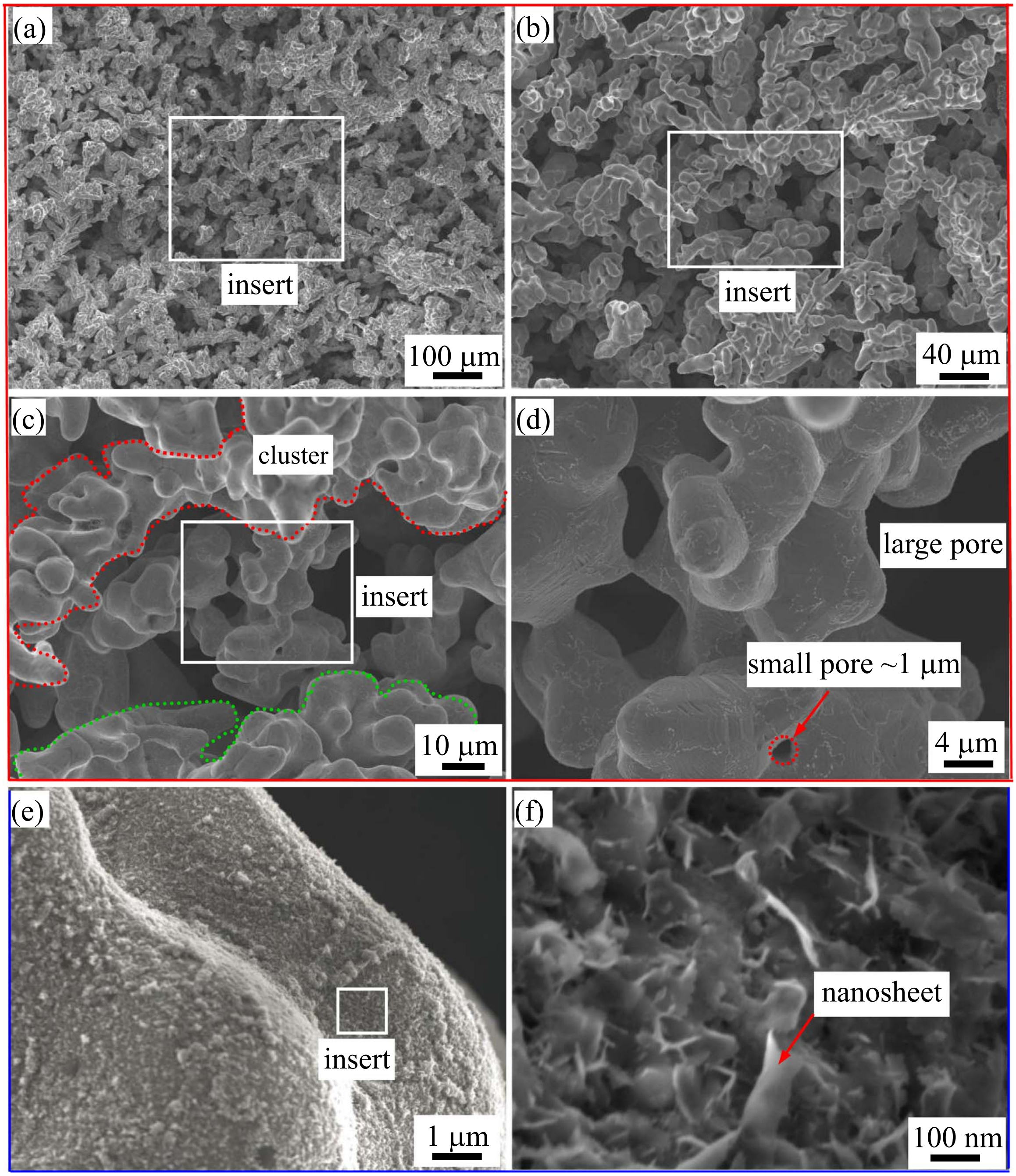

Fig. 5. SEM photos after the particle sintering (a–d for sintered porous without nano-structure, e and f for sintered particles with nano-sheet structure).

3. Results and discussion

Before the formal experiment on our heat pipes, we fabricated a vapor chamber heat pipe that is identical to that in Hwang et al. [29] to verify the reliability of our experimental setup and procedure. The wick fabrication, water charging and temperature measurements are all similar to those reported in the reference. The description of the heat pipe and experimental procedure can be seen in Supplementary Material. The following describes the results and discussion on our heat pipe samples.

3.1. Evaporator wall and vapor temperatures

During HP operation, evaporator wall temperature should be controlled because most of electronic chip specifies the temperature limit of 85 °C. Higher temperature exceeding this limit shortens the device lifetime [30]. Internal vapor temperature is also important because it corresponds to the vapor pressure. A suitable internal pressure is useful to balance the outside pressure to minimize the geometry deformation. Here, $T_{e,c}$ (evaporator center wall temperature) and T_v (vapor temperature) are plotted in Fig. 9 versus heat fluxes q_e (net heating load divided by the thin film heater area). Results are presented for the three HP samples with two typical HP orientations: bottom heating with θ=0° and top heating with θ=180°. Our measurements are well consistent with the analysis given in Section 2. The #1 sample with equal wettability match gave highest wall temperatures, while #3 sample with opposite wettability match yields the lowest wall temperatures. The #2 sample with moderate wettability difference lies in between #1 and 3 samples. Large $T_{e,c}$ difference was observed between #1 sample and the other two samples, indicating the

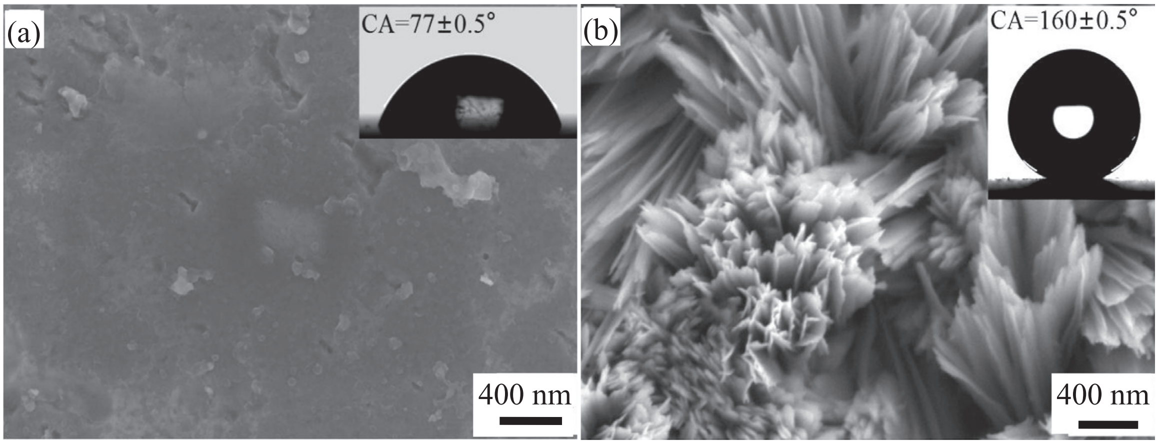

Fig. 6. SEM photos for hydrophilic condenser surface (a) and super-hydrophobic condenser surface with nano-flower structure (b).

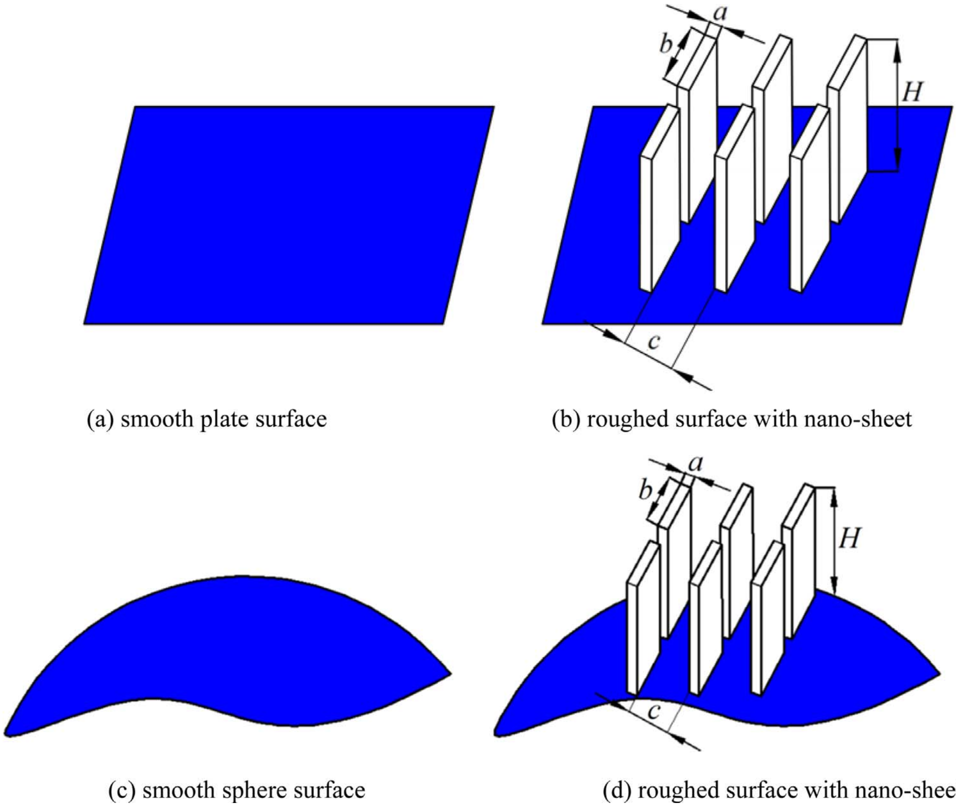

Fig. 7. Smooth and roughed surface. (a) smooth plate surface. (b) roughed surface with nano-sheet. (c) smooth sphere surface. (d) roughed surface with nano-sheet.

significance of nano-structured surface in porous wick, as well as on condenser surface. At q_e=100.3 W/cm^2, the #3 sample had $T_{e,c}$ of 65.9 °C, which was 37.3 °C lower than that for the #1 sample. The internal vapor temperatures T_v have similar response to heat fluxes as those of $T_{e,c}$ versus q_e (see Fig. 9b). Nano-structured surface in evaporator porous wick and/or on condenser surface not only suppresses wall temperatures, but also decreases internal vapor temperatures to limit the pressure. Besides, the #2 and #3 samples extend the heat flux range by about 40% compared with #1 sample. For example, #3 sample sustains heat flux of 142.5 W/cm^2 on a 1.4 cm^2 heater surface with $T_{e,c}$ of 80.0 °C. On the contrary, #1 sample sustains q_e of 100.3 W/cm^2 but with $T_{e,c}$ of 102.3 °C. Nano-structure in evaporator porous wick attracts water to prevent dry-out at high heat fluxes for evaporator, accounting for the extended heat flux range.

The weak influence of HP orientations on both $T_{e,c}$ and T_v is observed. For any HP sample, $T_{e,c}$ and T_v only show a couple of degrees difference between bottom and top heating modes. Fig. 10 gave the explanation. Similar to the effect of wettability combination of evaporator and condenser on heat pipe, the effect of heat pipe orientation on the performance is also related to phase distribution in the mastoid process and other void space not occupied by solid material. Keep in mind that the charged water thoroughly floods all the evaporator porous wick at adiabatic condition, heating the evaporator results in some vapor voids in the porous wick to expel the identical volume of water to outside of the porous wick. We consider the phase distribution inside the porous wick for different orientations first. Such distribution is related to the Bond number expressed as [31].

$$Bo = \frac{(\rho_l - \rho_v)gL^2}{\sigma} \tag{3}$$

where ρ is the density, g is the gravity acceleration, L is the

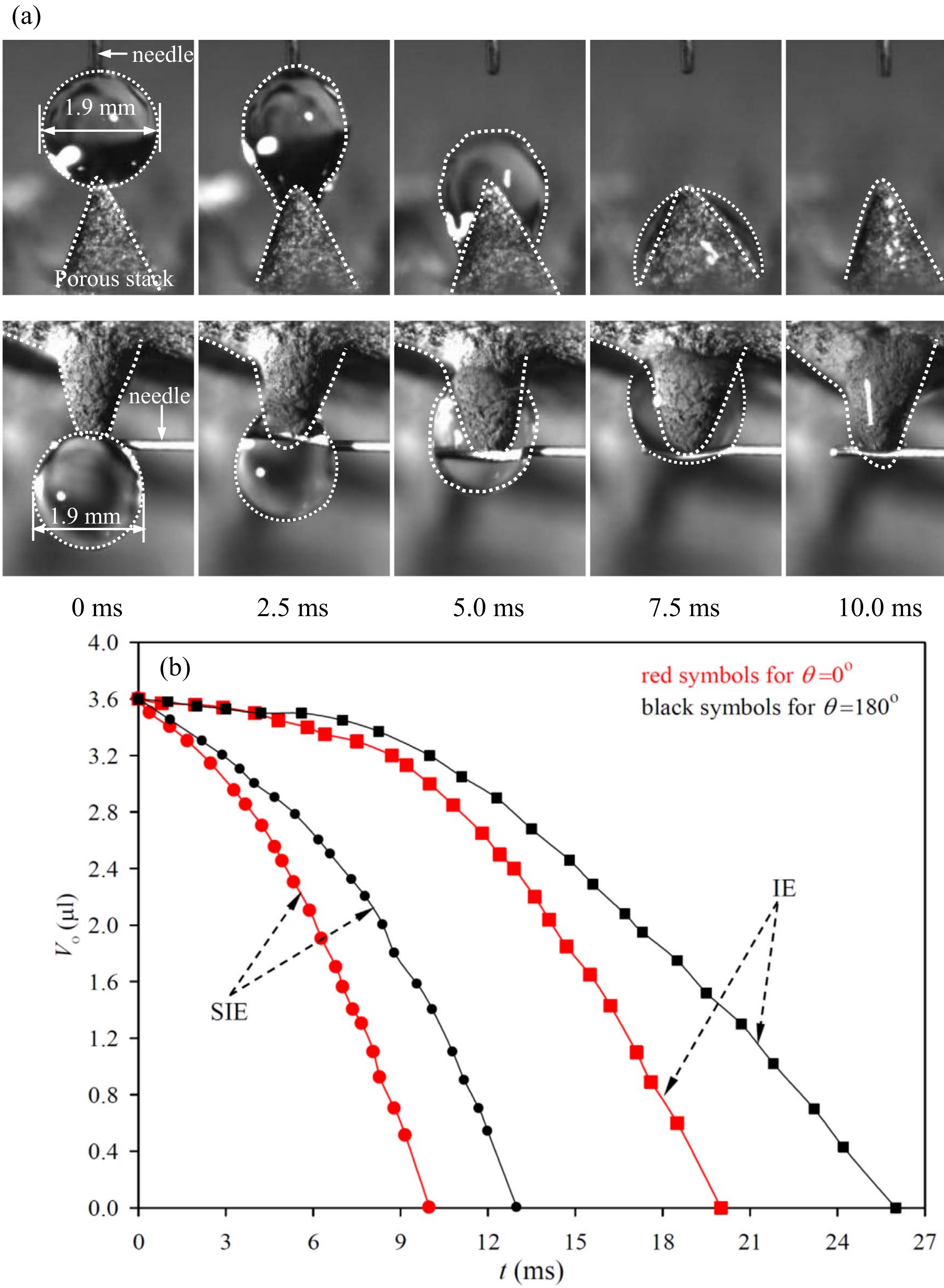

Fig. 8. Water drop suction process for hydrophilic mastoid process (IE) and super-hydrophilic mastoid process (SIE).

characteristic length and σ is the surface tension. Bond number represents the gravity force related to the surface tension force. We recall that there are two length scales for the sintered porous wick without nano-structure, and three length scales with nano-structure involved. The Bond number determined phase distribution in terms of micron, sub-micron or nano-meter is definitely a surface tension dominant process. Noting that there are larger pore channels or cavities in ~10–100 μm scale, we substitute L=100 μm in Eq. (3) to yield Bo=0.036. This estimation explains the insensitivity of phase distribution inside porous wick with respect to gravity force. That is to say, the phase distribution is similar for bottom and top heating modes.

The expelled water from inside to outside of the mastoid processes is identical for different orientations at heating condition. Then, phase distribution outside of the mastoid processes is dependent on the bulk driving force from evaporator to condenser. Even for the equal wettability combination of evaporator and condenser, the evaporator porous sub-layer is more hydrophilic than the condenser wall. The extra water may increase the water film thickness on the evaporator

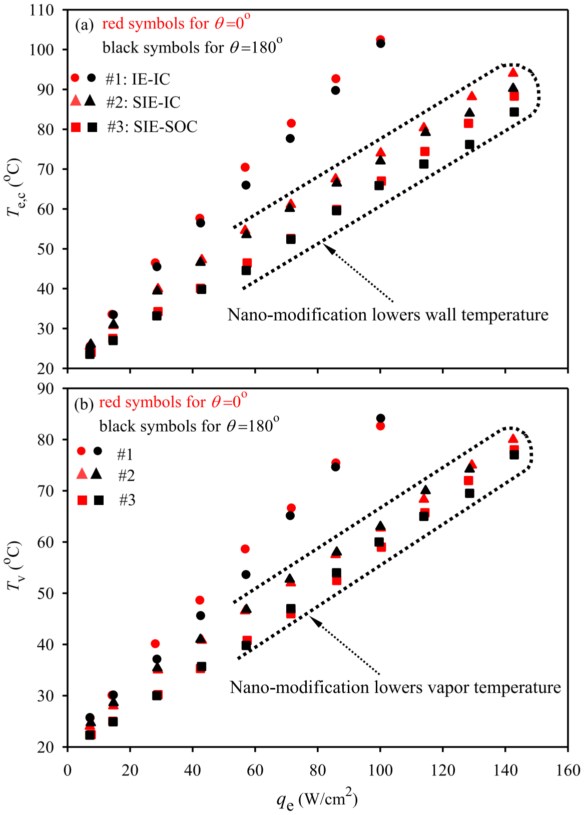

Fig. 9. Evaporator wall temperatures $T_{e,c}$ at the center and inside vapor temperatures T_v.

porous sub-layer, not on the condenser wall, explaining the weak effect of gravity force on heat pipe. The heat pipe can be arranged at any inclination angles for ground application, it can also be used in varied gravity acceleration environment for space application.

3.2. Switchable heat transfer mechanisms

We show the switch of two dominant heat transfer mechanisms for present heat pipes. Most studies used boiling curves to characterize the performance [32]. Here, we used both boiling curves (Fig. 11a), and boiling heat transfer coefficients (HTCs, see Fig. 11b). HTC is the slope of the boiling curves, identifying the boiling mechanisms. We note that Fig. 11 was obtained for heat pipes, not under pool boiling condition. The #1 sample behaves almost a linear curve of heat fluxes q_e against wall superheat ($T_{e,c}$-T_v), corresponding to HTCs not changed versus heat fluxes q_e to behave perfect convection heat transfer mechanism. On the other hand, the #2 and 3 HP samples display more steep slopes of boiling curves, corresponding to obvious rises of HTCs with increases in heat fluxes to show the nucleation mechanism. Fig. 11 shows significant differences of boiling performances between the three heat pipes. The difference became more significant for high heat fluxes (heating loads). The #1 sample weakly increased HTCs from 54.3 kW/m^{2}K at q_e=28.7 W/cm^2 to 57.9 kW/m^{2}K at q_e=100.3 W/cm^2. But, the #3 sample increased HTCs from 90.1 kW/m^{2}K at q_e=28.7 W/cm^2 to 194.8 kW/m^{2}K at q_e=142.8 W/cm^2. The HTC at q_e=142.8 W/cm^2 for #3 sample was 3.4 times of that at q_e=100.3 W/cm^2 for #1 sample. The HTCs for #2 sample are in between those of #1 and #3. Fig. 11c demonstrates similar change trends of condensation heat transfer coefficients (HTCs) versus heating load Q as to those shown in Fig. 11b. HTCs are not sensitive to Q for #1 sample, but are significantly increased versus Q for the other two HP samples, especially for #3 sample. Maximum HTC could be 8.3 kW/m^2 K for #3 sample, which was ~5 times of that for #1 sample.

The total thermal resistance, R=R_e+R_c, characterizes the global heat pipe performance, linking the evaporator and condenser. The lower the total thermal resistance, the better the heat pipe performance is. Fig. 12 shows R distribution for different heating loads Q at both bottom (θ=0°) and top (θ=180°) heating modes. The influence of gravity force on total resistances is weak. The R values are even slightly lower at the top heating mode than those at the bottom heating mode, consistent with the response of evaporator center wall temperatures $T_{e,c}$ with respect to inclination angles (see Fig. 9). The influence of wettability matches of evaporator and condenser are significant. At Q=20.2 W, the total thermal resistance for #3 sample was 0.4 times of that for #1 sample. At Q=140.4 W, the total thermal resistance for #3 sample was 1/3 of that for #1 sample. The nano-surface modification generates great benefit at high heating load.

Fig. 11 shows that heat transfer coefficient of evaporator is much larger than that of condenser, i.e. $h_e > h_c$. It seems that thermal resistance of evaporator should be smaller than that of condenser, i.e. $R_e < R_c$. But Fig. 12 shows that $R_e > R_c$. This inconsistence comes from the different heat transfer areas of heater and condenser. The supplementary material gave the data reduction of these parameters. For evaporator, thermal resistances and heat transfer coefficient are

$$R_e = \frac{(T_{e,c} - T_v)}{Q - Q_{loss}},\ h_e = \frac{Q - Q_{loss}}{A_{heater}(T_{e,c} - T_v)} \tag{4}$$

For condenser, the following equations exist

$$R_c = \frac{(T_v - T_{c,ave})}{Q - Q_{loss}},\ h_c = \frac{Q - Q_{loss}}{A_c(T_v - T_{c,ave})} \tag{5}$$

Thus, the following relationship exists

$$R_e = \frac{1}{A_{heater}h_e},\ R_c = \frac{1}{A_c h_c} \tag{6}$$

Attention should be paid on the heater area (A_{heater}=1.4 cm^2), and the condenser surface area (A_c= 69.4 cm^2). The fact of significantly larger A_c than A_{heater} caused $R_e > R_c$ (see Fig. 12). Evaporator contributes the major thermal resistance.

3.3. Analysis of the switch of two dominant heat transfer mechanisms

The introducing of concepts of continuous phase, disperse phase, thermally-controlled heat transfer and inertia-controlled heat transfer helps to understand the two dominant heat transfer mechanisms.

3.3.1. Nucleation mechanism for heat pipes

Super-hydrophilic evaporator and super-hydrophobic condenser (sample #3) hold the continuous phase of water inside evaporator porous wick, and continuous phase of vapor on condenser surface, under which isolated bubbles nucleate, grow and release out of evaporator porous wick to show nucleation mechanism. Bubbles are the dispersed phase in evaporator. Bubble nucleation is a periodic process to be thermally-controlled. Heat transfer coefficients are related to the number of active nucleation sites. Refs. [33,34] gave a well-known active bubble nucleation size range as

$$D_{c\ \max,\ \min} = \frac{\delta_t \sin\alpha}{2(1 + \cos\alpha)}\left(\frac{\Delta T}{\Delta T + \Delta T_{sub}}\right)\left[1 \pm \sqrt{1 - \frac{8\sigma(\Delta T + \Delta T_{sub})(1 + \cos\alpha)T_{sat}}{\rho_v i_{lv}\delta_t \Delta T^2}}\right] \tag{7}$$

where δ_t, α, σ, T_{sat}, ρ_v, i_{lv} are thermal boundary layer thickness, contact angle, surface tension, saturation temperature, vapor density and latent heat of evaporation, respectively. ΔT_{sub} is the liquid subcooling, which equals 0 for saturation boiling. ΔT is the wall superheat, equals to $T_{e,c}$–T_v in this study. Giving the values of α=1°, σ=0.0662 N/m, T_{sat}=333.15 K, ρ_v=0.13 kg/m^3, i_{lv}=2358.4 kJ/kg for water-vapor system, when the wall superheats ΔT are 1 K, 2 K, and 10 K such as

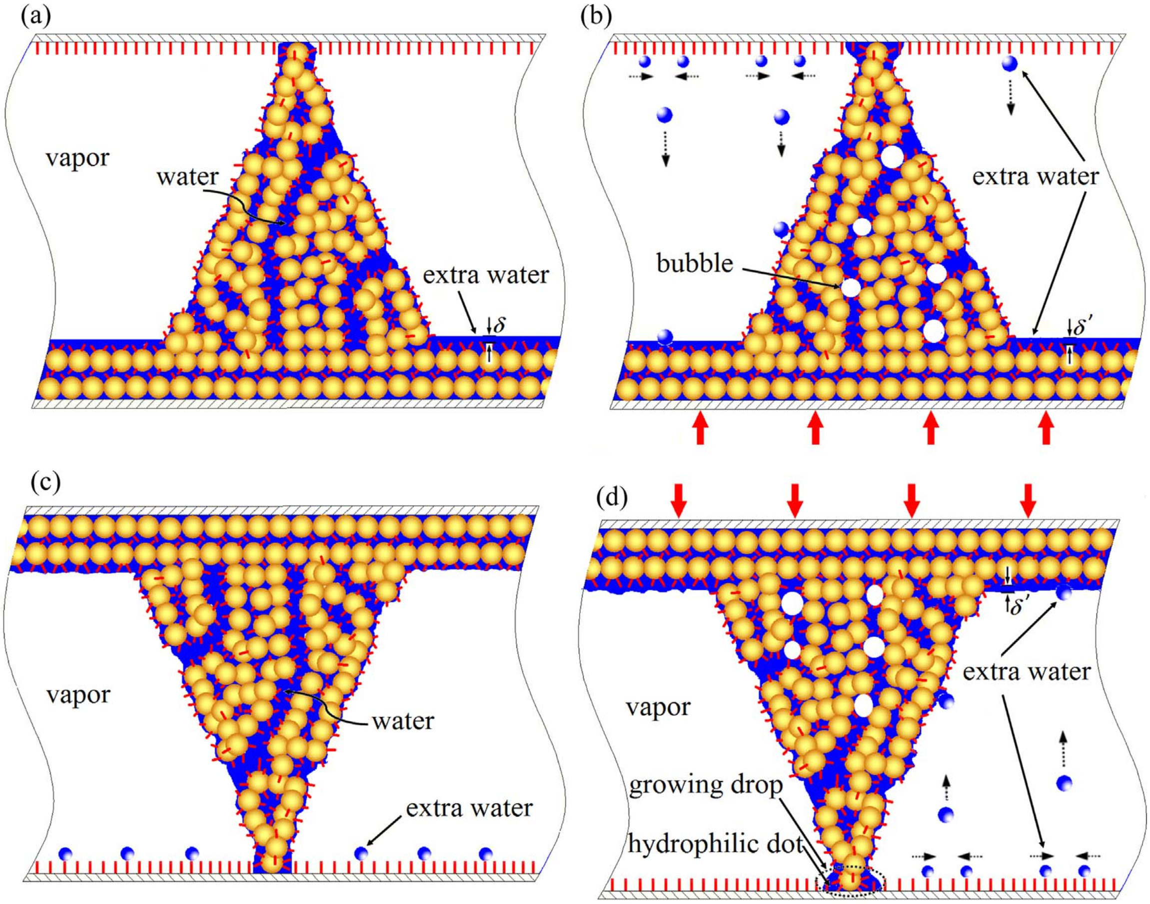

Fig. 10. Effect of heating on the phase distribution at the bottom and top heating modes (a: phase distribution at adiabatic condition; b: phase distribution at the bottom heating mode, bubble voids in pore channels expel extra water to increase the water film thickness $\delta > \delta'$, c: phase distribution at adiabatic condition; d: phase distribution at the top heating mode, bubble voids in pore channels expel extra water to increase the water film thickness $\delta > \delta'$, the junction points nucleate, grow and suck the water drop towards the porous wick of evaporator).

encountered in this study, the active nucleation size D_c are 3.17–12.00 μm, 1.42–10.62 μm, 0.26–6.78 μm, respectively. This estimation shows that the increased wall superheats at higher heat fluxes push the active bubble nucleation size to be smaller. Some pore cavities are not active at small heat flux, but become active at higher heat flux. The evaporator porous wick contains large quantity of pore cavities in micron scale. More pore cavities are available to be nucleation sites when heat fluxes are increased, leading to increased slopes of boiling curves to demonstrate smart response of heat transfer coefficients with respect to heat fluxes.

Ćoso et al. [35] examined biporous media consisting of microscale pin fins separated by microchannels as candidate evaporator structure for vapor chamber heat pipes. Pores which separate microscale pin fins are used to generate high capillary suction, while larger microchannels are used to reduce overall flow resistance. They observed both the nucleate boiling and evaporation phenomena, depending on the pin fin structure parameters. They identified the transition from evaporation to nucleate boiling. For the evaporation dominant heat transfer, the heat flux reached 119.6 W/cm^2, while the nucleate boiling extended the heat flux up to 277.0 W/cm^2. They examined the suppression of evaporation due to reduction in pore scale.

Tsai et al. [36] investigated two-phase closed thermosyphon vapor-chamber system. They found that the heat transfer mechanism of the three surfaces all can be ranked as boiling dominated. Lips et al. [37] investigated nucleate boiling in a flat grooved heat pipe and emphasized the importance of nucleate boiling on heat pipe performance. They wrote "The presence of nucleate boiling in the grooves improves the thermal performance of the flat heat pipe". In the conclusion section, they wrote "The experiments show that boiling does not prevent the operation of the flat plate heat pipe even in presence of fully developed boiling phenomenon, but on the contrary, improves the heat transfer".

For opposite wettability match of evaporator and condenser (#3 sample), regarding the condenser surface, the continuous and disperse phases are vapor and condensed drops, respectively. Graham and Griffith [38] assumed the minimum radius r_{min} of the droplets to be equal to the critical radius r_0, which can be obtained from the classical heterogeneous droplet nucleation.

$$r_{\min} = r_0 = \frac{2\sigma T_{Sat}}{\rho_l i_{lv} \Delta T_{sub}} \tag{8}$$

where $\Delta T_{\text{sub}} = T_{\text{v}} - T_{\text{c}}$ is the condenser wall subcooling, T_{v} and T_{c} are the saturation vapor temperature and condenser wall temperature, respectively. Eq. (8) told us that, at the vapor temperature of 333.15 K (60 °C) and wall subcoolings of 1 K, 2 K, and 10 K, $r_{\min}$ (or r_0) are 190 nm, 95 nm and 19 nm, respectively. Our nano-structure surface contains such nano size range (see Fig. 6b). However, larger heat flux causes increased wall subcoolings to push the nucleation size much smaller. Small nanopores such as ~20 nm are not active at ΔT_{sub}=1 K but are active at ΔT_{sub}=10 K. Rose [17] gave the droplet number density N_{s} as

$$N_s = \frac{0.037}{r_{\min}^2} \tag{9}$$

Eq. (9) told us that active nucleation sizes are significantly reduced, drop number densities are sharply increased when wall subcoolings are increased due to the raised heat fluxes. Thus, the nucleation heat

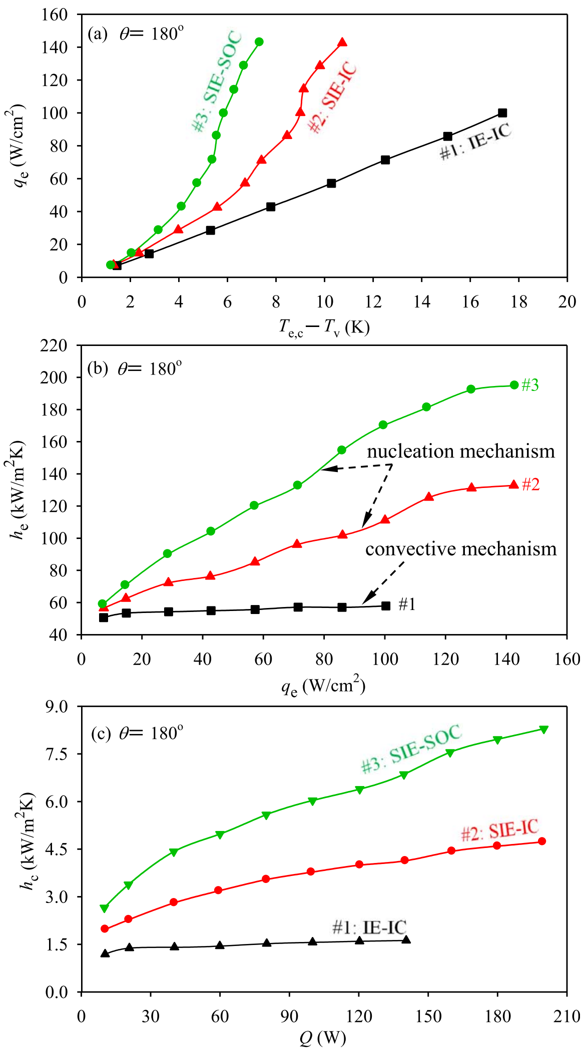

Fig. 11. Boiling curves and heat transfer coefficients for evaporator and condenser.

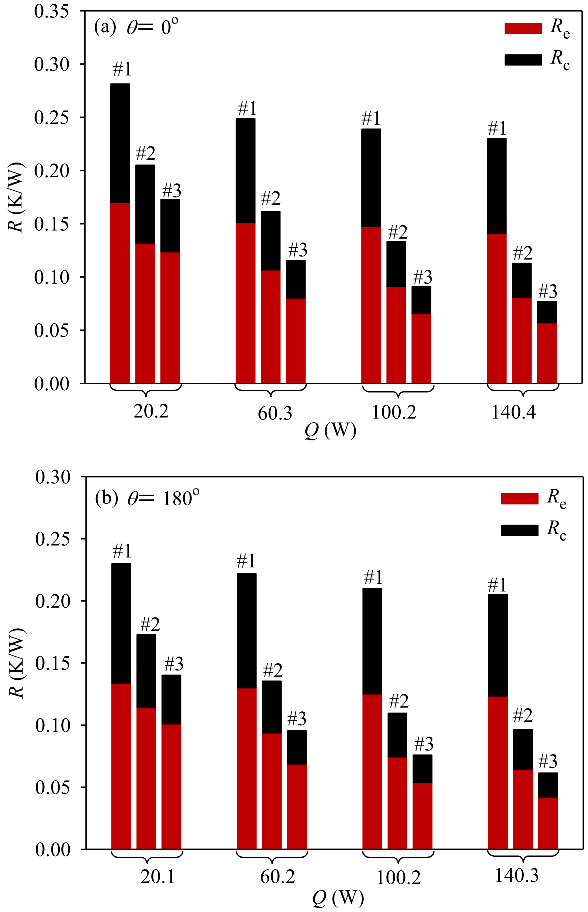

Fig. 12. Overall thermal resistances for three different wettability matches of evaporator and condenser.

transfer coefficients obviously increase by increasing heat fluxes. Nucleation heat transfer coefficients are controlled by thermal non-equilibrium effect.

3.3.2. Convection mechanism for heat pipes

For #1 sample, the global driving force by capillary pressure is reduced to cause some pore cavities in porous wick occupied by vapor, while extra water stays on the condenser surface. In evaporator, due to the imbalance of capillary pressures between small pores (~1 µm scale) and larger pores (~10–100 µm), small pores are still occupied by water, but vapor is the continuous phase in larger pore channels. Water-vapor interface is formed along the larger pore channels, on which steady convective evaporation happens. Intensity of the inertia-controlled convection heat transfer is related to the shear stress at the water-vapor interface. Heat transfer coefficient is determined by the water film thickness underneath the bulk vapor cloud. We shall note that the convective evaporation in this paper is different from the (vapor) film heat transfer, for which a vapor layer on heating surface deteriorates heat transfer to behave post-dryout mode (Leidenfrost effect [39,40]).

Keep in mind that shear stress on the water-vapor interface and water film thickness are determined by vapor phase velocity u_v in larger pore channels, we analyze how u_v changes versus heating load Q. For steady HP operation, evaporation rate m (kg/s unit) is $m=Q/i_{lv}$. The latent heat of evaporation i_{lv} is not sensitive to the saturation vapor temperature. For #1 sample, when q_e is changed from 28.7 W/cm^2 to 100.3 W/cm^2, T_v is increased from 37.1 °C to 84.2 °C (see Fig. 9b). Correspondingly, i_{lv} is 2412.9 kJ/kg at T_v=37.1 °C and 2297.4 kJ/kg at T_v=84.2 °C. The i_{lv} values are only changed by 4.78% at the two vapor temperatures. The following expression exists by using the mass conservation equation of $m=N_p \rho_v u_v A_p$.

$$u_v = \frac{1}{N_p A_p} \times \frac{1}{i_{lv}} \times \frac{Q}{\rho_v} \tag{10}$$

where N_p, A_p, ρ_v are number of total evaporator pore channels (~10–100 µm scale), cross section area of one pore channel, and vapor density, respectively. Due to the weak change of i_{lv}, Eq. (10) shows that u_v can be scaled as $u_v \sim Q/\rho_v$. For #1 sample, when q_e is changed from 28.7 W/cm^2 to 100.3 W/cm^2, T_v is increased from 37.1 °C to 84.2 °C (see Fig. 9b). Vapor densities ρ_v are increased from 0.0448 kg/m^3 to 0.3474 kg/m^3. The sharp increase of ρ_v versus Q significantly suppresses the rise of vapor velocities, accounting for insensitive response of water film thickness and heat transfer coefficients with respect to heat fluxes.

Up to now, we discussed nucleation heat transfer for #3 sample and convection heat transfer for #1 sample. Compared with #3 sample, the #1 sample reduced bulk driving force from condenser to evaporator. Some part of larger pore channels is occupied by vapor to weaken the nucleation effect. The #2 sample behaves the hybrid mechanisms of nucleation and convection, but still displays nucleation characteristic to have increased HTCs versus Q. The two mechanisms were also found in our previous study on the forced convective boiling in microchannels [41]. Recently, Ćoso et al. [35] showed that both nucleate boiling and thin liquid film evaporation can happen for pool boiling.

3.3.3. Comments on the heat pipe structure

Evaporator and condenser are two major components for HP. The mastoid process array holds several length scales. The ~mm scale base diameter and height of mastoid process provide significantly extended fin area to enhance heat transfer, which is a big benefit compared with any plain surface. The mastoid process is a biporous wick to contain many small pores for capillary generation/bubble nucleation and larger pores for viscous reduction.

Our #3 HP sample contains junction points array on condenser wall, behaving distinct feature compared with other HP designs in the literature. The mastoid process tip is super-hydrophilic. Thus, the condenser wall is a heterogeneous surface with ordered super-hydrophilic dots on super-hydrophobic wall (see Fig. 10d). The heterogeneous surface helps to activate droplet nucleation at small wall subcooling. Recent study shows that the heterogeneous surface can prevent or delay the water flooding on the surface [42].

Finally, we talk about the water return path from condenser to evaporator. We mentioned that the junction points are preferred to be active droplet nucleation sites. Water drops grow there and quickly sucked towards evaporator porous wick, being an important water return path. Other locations except the tip junctions can also be active droplet nucleation sites, especially at higher wall subcoolings. Growing droplets result in coalescence induced jumping, which was investigated by many authors [43–45]. If condenser is above evaporator, any droplets departing from condenser can be captured by evaporator porous wick with the help of gravity. If condenser is below evaporator, the success droplet capture depends on jumping velocity and height. During droplet coalescence, part of surface energy is converted to kinetic energy. Too small drops such as radius smaller than 10–20 μm cannot jump [46]. Liu et al. [47] showed that jumping heights are sharply increased for droplet radius increased from 10 μm to 68 μm. The maximum jumping height is 1.75 mm at the drop radius of 68 μm, beyond which jumping heights are slightly decreased. Our heat pipe had a 1.5 mm internal thickness to match droplet jumping height for success capture. We note that the conical mastoid process obviously shortens the necessary jumping height. Jumping droplets can be captured by the inclined porous surface (see Fig. 10d).

4. Conclusions

Boiling and condensing are coupled in a heat pipe. The novel concept of this paper focused on the management of the phase distribution by nano-surface modification on sintered particle surface and/or condenser surface. Because nucleation mechanism ensures increased heat transfer coefficients versus heat fluxes, the objective is to suppress convection effect but maintain nucleation mechanism. An optimal water charge ratio should be searched for the switchable heat transfer mechanisms. Three heat pipe samples were fabricated. The #1 sample did not contain nano-surface to behave limited driving force for water circulation from condenser to evaporator. Convection evaporation happens on the vapor-liquid interface in pore channels of evaporator porous wick, and convection (filmwise) condensing occurs on the condenser surface. Our analysis shows that when heat fluxes are increased, the increased vapor densities suppress the rise of vapor velocities on the vapor-liquid interface, accounting for quasi-constant heat transfer coefficients. The super-hydrophilic evaporator and super-hydrophobic condenser (#3 sample) hold nucleation mechanism with obviously increased heat transfer coefficients versus heat fluxes, explained by more active nucleation sites at high heat fluxes. The #3 sample had its global thermal resistance of 1/3 to that of the #1 sample. Evaporator wall temperatures are decreased by 30–40 °C at high heat fluxes such as ~100 W/cm^2, via the nano-surface modification. The benefit of micro/nano structure for HP and the water return path are discussed in this paper.

Acknowledgements

This work is supported by the National Natural Science Foundation of China (51676071), the Key Project of Natural Science Foundation of China (51436004).

Appendix A. Supplementary material

Supplementary data associated with this article can be found in the online version at doi:10.1016/j.nanoen.2017.06.010.

References

[1] K.S. Yang, C.H. Chung, M.T. Lee, S.B. Chiang, C.C. Wong, C.C. Wang, An experimental study on the heat dissipation of LED lighting module using metal/carbon foam, Int. Commun. Heat. Mass 48 (2013) 73–79.

[2] I. Mudawar, M.B. Bowers, Ultra-high critical heat flux (CHF) for subcooled water flow boiling–I: chf data and parametric effects for small diameter tubes, Int. J. Heat. Mass Transf. 42 (1999) 1405–1428.

[3] M.M. Rahman, J. Dongxu, M.S. Beni, H.C. Hei, W.D. He, J.Y. Zhao, Supercritical water heat transfer for nuclear reactor applications: a review, Ann. Nucl. Energy 97 (2016) 53–65.

[4] N.A. Patankar, Supernucleating surfaces for nucleate boiling and dropwise condensation heat transfer, Soft Matter 6 (2010) 1613–1620.

[5] C.M. Patil, S.G. Kandlikar, Review of the manufacturing techniques for porous surfaces used in enhanced pool boiling, Heat. Transf. Eng. 35 (2014) 887–902.

[6] B.S. Kim, G. Choi, S. Shin, T. Gemming, H.H. Cho, Nano-inspired fluidic interactivity for boiling heat transfer: impact and criteria, Sci. Rep. 6 (2016) 34348.

[7] K.O. Zamuruyev, H.K. Bardaweel, C.J. Carron, N.J. Kenyon, O. Brand, J.P. Delplanque, C.E. Davis, Continuous droplet removal upon dropwise condensation of humid air on a hydrophobic micropatterned surface, Langmuir 30 (2014) 10133–10142.

[8] B. Bourdon, R. Rioboo, M. Marengo, E. Gosselin, J. De Coninck, Influence of the wettability on the boiling onset, Langmuir 28 (2012) 1618–1624.

[9] H.C. Jin, G.P. Lin, L.Z. Bai, A. Zeiny, D.S. Wen, Steam generation in a nanoparticle based solar receiver, Nano Energy 28 (2016) 397–406.

[10] R.F. Wen, Q. Li, J.F. Wu, G.S. Wu, W. Wang, Y.F. Chen, X.H. Ma, D.L. Zhao, R.G. Yang, hydrophobic copper nanowires for enhancing condensation heat transfer, Nano Energy 33 (2017) 177–183.

[11] X.Y. Lu, T.C. Hua, M.J. Liu, Y.X. Cheng, Thermal analysis of loop heat pipe used for high-power LED, Thermochim. Acta 493 (2009) 25–29.

[12] T. Semenic, I. Catton, Experimental study of biporous wicks for high heat flux applications, Int. J. Heat. Mass Transf. 52 (2009) 5113–5121.

[13] S.C. Shena, H.J. Huanga, J.C. Hsieh b, H.J. Shaw, Self-adaptive heat spreader with a micromesh using LIGA-like technology for AUV LED headlight, Appl. Ocean Res. 32 (2010) 137–145.

[14] Y.L. Ji, H.H. Chen, Y.J. Kim, Q.S. Yu, X.H. Ma, H.B. Ma, Hydrophobic surface effect on heat transfer performance in an oscillating heat pipe, J. Heat. Transf. 134 (2012) 074502.

[15] F.Z. Zhang, R.A. Winholtz, W.J. Black, M.R. Wilson, H. Taub, H.B. Ma, Effect of hydrophilic nanostructured cupric oxide surfaces on the heat transport capability of a flat-plate oscillating heat pipe, J. Heat. Transf. 138 (2016) 062901.

[16] J.B. Boreyko, C.H. Chen, Vapor chambers with jumping-drop liquid return from superhydrophobic condensers, Int. J. Heat. Mass Transf. 61 (2013) 409–418.

[17] J.W. Rose, Further aspects of dropwise condensation theory, Int. J. H. Eat. Mass Transf. 19 (1976) 1363–1370.

[18] X.B. Ji, J.L. Xu, Z.W. Zhao, W.L. Yang, Pool boiling heat transfer on uniform and non-uniform porous coating surfaces, Exp. Therm. Fluid Sci. 48 (2013) 198–212.

[19] R. Xiao, S.C. Maroo, E.N. Wang, Negative pressures in nanoporous membranes for thin film evaporation, Appl. Phys. Lett. 102 (2013) 123103.

[20] J. Kim, Review of nucleate pool boiling bubble heat transfer mechanisms, Int. J. Multiph. Flow. 33 (2009) 691–706.

[21] C. Li, Z.K. Wang, P.I. Wang, Y. Peles, N. Koratkar, G.P. Peterson, Nanostructured copper interfaces for enhanced boiling, Small 4 (2008) 1084–1088.

[22] X.L. Liu, P. Cheng, Dropwise condensation theory revisited Part II. Droplet nucleation density and condensation heat flux, Int. J. Heat. Mass Transf. 83 (2015) 842–849.

[23] N. Miljkovic, E.N. Wang, Condensation heat transfer on superhydrophobic surfaces, MRS Bull. 38 (2013) 397–406.

[24] K. Koch, W. Barthlott, Superhydrophobic and superhydrophilic plant surfaces: an inspiration for biomimetic materials, Philos. Trans. Roy. Soc. A 367 (2009) 1487–1509.

[25] B. Bhushan, Biomimetics: lessons from nature-an overview, Philos. T. Roy. Soc. A 367 (2009) 1445–1486.

[26] J. Feng, Y. Pang, Z. Qin, R. Ma, S. Yao, Why condensate drops can spontaneously move away on some super-hydrophobic surfaces but not on others, ACS Appl. Mater. Interfaces 4 (2012) 6618–6625.

[27] X. Yao, Q. Chen, L. Xu, Q. Li, Y. Song, X. Gao, D. Quéré, L. Jiang, Bioinspired ribbed nanoneedles with robust superhydro-phobicity, Adv. Funct. Mater. 20 (2010) 656–662.

[28] R.N. Wenzel, Resistance of solid surfaces to wetting by water, J. Ind. Eng. Chem. 28 (1936) 988–994.

[29] G.S. Hwang, Y. Nam, E. Fleming, P. Dussinger, Y.S. Ju, M. Kaviany, Multi-artery heat pipe spreader: experiment, Int. J. Heat. Mass Transf. 53 (2010) 2662–2669.

[30] S.C. Wong, S.F. Huang, K.C. Hsieh, Performance tests on a novel vapor chamber, Appl. Therm. Eng. 31 (2011) 1757–1762.

[31] W.H. Hager, Wilfrid Noel Bond and the Bond number, J. Hydraul. Res. 50 (2012) 3–9.

[32] S. Mori, K. Okuyama, Enhancement of the critical heat flux in saturated pool boiling using honeycomb porous media, Int. J. Multiph. Flow. 35 (2009) 946–951.

[33] Y.Y. Hsu, On the size range of active nucleation cavities on a heating surface, J. Heat. Transf. 84 (1962) 207–216.

[34] F. Yang, X. Dai, Y. Peles, P. Cheng, J. Khan, C. Li, Flow boiling phenomena in a single annular flow regime in microchannels (I): characterization of flow boiling heat transfer, Int. J. Heat. Mass Transf. 68 (2014) 703–715.

[35] D. Ćoso, V. Srinivasan, M.C. Lu, A. Majumdar, Enhanced heat trnasfer in biporous wicks in the thin liquid film evaporation and boiling regimes, J. Heat. Transf. 134 (2012) 101501.

[36] T.E. Tsai, H.H. Wu, C.C. Chang, S.L. Chen, Two-phase closed thermosyphon vapor-chamber system for electronic cooling, Int. Commun. Heat. Mass 37 (2010) 484–489.

[37] S. Lips, F. Lefevre, J. Bonjour, Nucleate boiling in a flat grooved heat pipe, Int. J. Therm. Sci. 48 (2009) 1273–1278.

[38] C. Graham, P. Griffith, Drop size distributions and heat transfer in dropwise condensation, Int. J. Heat. Transf. 16 (1973) 337–346.

[39] B.S. Gottfried, C.J. Lee, K.J. Bell, The Leidenfrost Phenomenon: film boiling of liquid droplets on a flat plate, Int. J. Heat. Mass Transf. 9 (1966) 1167–1187.

[40] I.U. Vakarelski, N.A. Patankar, J.O. Marston, D.Y.C. Chan, S.T. Thoroddsen, Stabilization of leidenfrost vapour layer by textured superhydrophobic surfaces, Nature 489 (2012) 274–277.

[41] J.L. Xu, S. Shen, Y.H. Gan, Y.X. Li, W. Zhang, Q.C. Su, Transient flow pattern based microscale boiling heat transfer mechanisms, J. Micromech. Microeng. 15 (2005) 1344–1361.

[42] T. Furuta, M. Sakai, T. Isobe, A. Nakajima, Effect of dew condensation on the wettability of rough hydrophobic surfaces coated with two different silanes, Langmuir 26 (2010) 13305–13309.

[43] J.B. Boreyko, Y.J. Zhao, C.H. Chen, Planar jumping-drop thermal diodes, Appl. Phys. Lett. 99 (2011) 234105.

[44] K. Rykaczewski, A.T. Paxson, S. Anand, X.M. Chen, Z.K. Wang, K.K. Varanasi, Multimode multidrop serial coalescence effects during condensation on hierarchical superhydrophobic surfaces, Langmuir 29 (2013) 881–891.

[45] N. Miljkovic, R. Enright, Y. Nam, K. Lopez, N. Dou, J. Sack, E.N. Wang, Jumping-droplet-enhanced condensation on scalable superhydrophobic nanostructured surfaces, Nano Lett. 13 (2013) 179–187.

[46] T.Q. Liu, W. Sun, X.Y. Sun, H.R. Ai, Mechanism study of condensed drops jumping on super-hydrophobic surfaces, Colloids Surf. 414 (2012) 366–374.

[47] X.L. Liu, P. Cheng, X.J. Quan, Lattice Boltzmann simulations for self-propelled jumping of droplets after coalescence on a superhydrophobic surface, Int. J. Heat. Mass Transf. 73 (2014) 195–200.

Dr. Xianbing Ji is currently an Associate Professor at North China Electric Power University, Beijing, China. He received his Ph.D. in 2009 in Guangzhou Institute of Energy Conversion, Chinese Academy of Science, Guangzhou, China. After that, he became a lecturer in North China Electric Power University. His current research focuses on phase-change heat transfer at macro/mini/nano-scale and heat exchanger improvement.

Dr. Jinliang Xu is the Dean of School of Mechanical and Power Engineering, North China Electric Power University, China. His research interest focuses on micro/nano heat transfer, micro energy system, and multiphase flow and heat transfer. He published more than 100 papers in recognized academic journals. He served as International conference chair or co-chair for several times in related area.

Hongchuan Li is a student in North China Electric Power University, China. His current research focuses on micro/nanoscale thermal and fluid transport and phase change, and electronic components cooling.

Dr. Guohe Huang holds BSC from Peking University (China), MSc from Simon Fraser University (Canada) and PhD from McMaster University (Canada). Since the 1990s, Huang has led over 150 environment-related research projects, produced over 800 peer-refereed international journal papers (with an SCI-based H-index of 54 in Science Citation Index under Thomson Reuters' Web of Science). He is a Fellow of the Canadian Academy of Engineering, and the President of the International Society for Environmental Information Sciences. He also acts (or acted) as editor-in-chief for 2 international journals and editorial board member for over 10 journals.